Research Article Vol. 34, No. 4 / 23 Feb 2026 / *Optics Express* 6296

Optics EXPRESS

Ultrashort-pulse optical manipulation of anisotropic nanoparticles via photonic nanojets and hooks in aqueous environments

MAYA HEN SHOR PELED[1] **AND ALINA KARABCHEVSKY**[1,2,*]

[1] *School of Electrical and Computer Engineering, Ben-Gurion University of the Negev, Beer-Sheva 8410501, Israel*
[2] *Department of Physics, Lancaster University, LA1 4YB, United Kingdom*
[*] *alinak@bgu.ac.il*

Abstract: We present a computational study on the optical manipulation of anisotropic gold nanoparticles, rods, and disks in aqueous environments using ultrashort pulsed photonic nanojets and photonic hooks. Using three-dimensional finite-difference time-domain simulations and analytical models of anisotropic polarizability, we analyze how shape, orientation, and surrounding medium influence the optical force landscape. Our results show that deviations from spherical particle geometry introduce strong orientation dependence, with optical forces varying by up to a factor of 5-10 across particle orientations and structured-field configurations. In particular, force minima emerge at intermediate tilt angles due to destructive coupling between polarizability axes. We also demonstrate that the surrounding medium significantly alters field confinement and force magnitude, with water enhancing field localization and modifying the dominant particle geometry. These findings provide design guidelines for structured-light-based nanoparticle manipulation, particularly for applications in nanomedicine, sensing, and fabrication, where real-world particles are non-spherical and operate in aqueous conditions.

1. Introduction

Optical manipulation, the use of light to exert forces on matter, has transformed how researchers probe and control microscopic systems and has enabled key advances in biomedical research, targeted drug delivery, and nanoscale assembly. While optical tweezers offer precise control over micron-scale objects using tightly focused beams [1], their effectiveness declines at the nanoscale due to the rapid decrease of optical force with particle volume and the diffraction limit [2,3]. Manipulating subwavelength particles such as proteins, viruses, and metal nanoparticles requires auxiliary structures that generate strongly confined optical fields. Stable trapping in aqueous media is further challenged by Brownian motion and weak confinement, particularly in the Rayleigh regime [4].

Near-field optical techniques, including plasmonic tweezers and photonic crystal resonators, overcome the diffraction limit by leveraging strong field enhancement [5–15]. However, their reliance on high-intensity continuous wave illumination can cause excessive photothermal heating, limiting their compatibility with biological samples [16]. Metamaterial-based optical tweezers offer advanced beam shaping and subwavelength confinement [17], but their complex fabrication and limited thermal robustness, especially in aqueous environments, hinder widespread application.

To address these limitations, alternative strategies have focused on reducing thermal load while maintaining effective optical trapping. Among them, pulsed illumination has emerged as a promising approach: by allowing thermal relaxation between pulses, it mitigates cumulative heating and reduces damage to sensitive samples [18–20].

#587041 https://doi.org/10.1364/OE.587041
Journal © 2026 Received 8 Dec 2025; revised 15 Jan 2026; accepted 20 Jan 2026; published 11 Feb 2026

In parallel, all-dielectric systems based on photonic nanojets (PNJs) have gained attention for their ability to confine light below the wavelength. PNJs are highly focused beams generated by dielectric microspheres or microcylinders that can trap and manipulate nanoparticles in a label-free and fabrication-friendly manner [21–26]. Their compatibility with pulsed sources and their ability to produce intense optical hotspots make them particularly attractive for thermally sensitive biological applications. Furthermore, when the symmetry of the illumination is broken, such as by partially obstructing the beam with a metallic structure, the beam curves into a photonic hook (PH), enabling directional control over nanoparticle motion [27].

In this study, we investigate optical manipulation of gold nanospheres, rods, and disks using PNJs and PHs formed by a dielectric microcylinder with and without an obstructing metallic plate, as seen in Fig. 1. We employ pulsed excitation with 100 femtosecond pulses spaced by 10 nanoseconds to ensure strong forces while minimizing thermal effects.

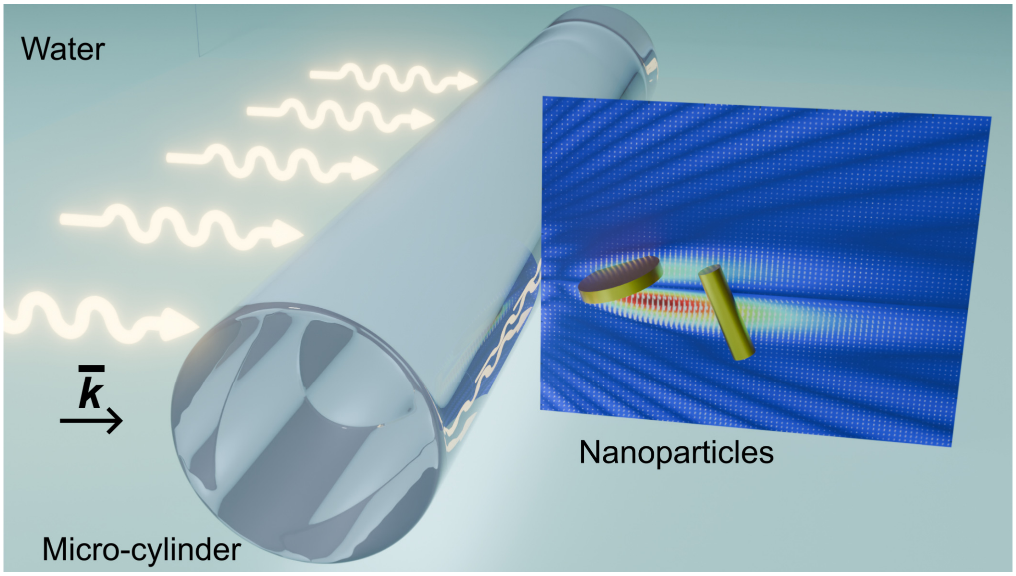

Fig. 1. Artistic illustration of the studied system. A pulsed excitation illuminates a dielectric microcylinder immersed in water, generating a photonic nanojet. If a metallic plate were added to partially obstruct the illumination, the field distribution would bend into a photonic hook. The structured light interacts with anisotropic gold nanoparticles (rods and disks), which are the focus of this study.

Nonspherical nanoparticles introduce intrinsic anisotropy, giving rise to orientation-dependent optical responses. Experimental work with dual-beam optical tweezers has shown that the alignment of nanorods significantly influences optical interactions and enables patterned assembly [28]. The anisotropic polarizability of gold nanorods has been well characterized in both single-particle and ensemble systems, revealing enhanced coupling to polarized fields and orientation-sensitive trapping behavior [29–31]. Even small deviations from spherical symmetry can significantly alter how particles couple to structured fields, yet the role of geometry and tilt in modulating optical forces remains underexplored.

We use full three-dimensional finite-difference time-domain (FDTD) simulations to compute the spatiotemporal electromagnetic fields and evaluate the optical forces using the electric dipole approximation. We analyze how particle geometry, orientation, and surrounding medium (air versus water) influence the optical force landscape. Our results show that rods and disks exhibit strongly orientation-dependent behavior governed by the projection of anisotropic polarizability onto spatially structured fields.

This work establishes a computational framework for modeling optical manipulation of anisotropic nanoparticles in aqueous environments. It provides design insights for structured-light systems in biomedical, sensing, and nanofabrication contexts, particularly where geometric, thermal, and fluidic constraints must be addressed jointly.

2. Methods

Our system is illuminated by a pulsed light source centered at a wavelength of 550 nm. This wavelength was selected to optimize the optical forces on gold nanoparticles in water, as the imaginary part of their polarizability, responsible for scattering forces, peaks near this value for 25 nm radius spheres. The electromagnetic fields are simulated using the finite-difference time-domain (FDTD) method in Ansys Lumerical, with perfectly matched layer (PML) boundary conditions applied to suppress reflections at the simulation boundaries. The scattered field formulation is employed, where a plane wave propagates along the x-axis and the electric field is polarized along the y-axis. All simulations are performed in three dimensions.

The dielectric micro-cylinder has a radius of 1 μm, a height of 2 μm, and a refractive index of 1.6, corresponding to SU-8 photoresist for its ease of fabrication, as described in Ref. [32]. The metallic plate is modeled as a perfect electric conductor (PEC) with dimensions of 0.5 μm in width, 1.5 μm in length, and 2 μm in height.

The system is illuminated by an unchirped Gaussian pulse with a full width at half maximum (FWHM) duration of 100 fs, corresponding to a spectral bandwidth of approximately 4.4 THz at a central wavelength of 550 nm. A temporal offset of 300 fs is applied to ensure the pulse is fully contained within the simulation window. A mesh size of 0.01 μm is used along the x- and y-directions to ensure accurate spatial resolution, and a field-time monitor is used to record the temporal evolution of the electromagnetic fields. The incident field amplitude is set to 2 MV/m to represent the pulsed illumination. Although the electromagnetic response of the system is linear, the simulations are performed fully in the time domain using a femtosecond pulse excitation. Optical forces are calculated from the instantaneous fields and integrated over the pulse duration, yielding an impulsive force rather than a time-averaged CW force.

We illuminate gold nanoparticles of different geometries, spheres, rods, and disks, under pulsed light. The optical forces acting on the nanoparticles are calculated within the electric dipole approximation, as their dimensions are much smaller than the incident wavelength ($\lambda_0 = 550$ nm). The spherical nanoparticle has a radius of $R = 25$ nm. The disk-shaped particle is designed with a radius larger than its height, specifically $R = 25$ nm and $h = 5$ nm. The rod-shaped particle is modeled with $R = 5$ nm and $h = 50$ nm. The optical force acting on a subwavelength particle in the dipole approximation is given by

$$\vec{F}(t) = (\vec{p} \cdot \nabla)\vec{E}(t) + \dot{\vec{p}}(t) \times \vec{B}(t), \tag{1}$$

where $\vec{p}$ is the electric dipole moment of the particle, $\dot{\vec{p}}$ is its time derivative, and $\vec{E}$ and $\vec{B}$ are the local electric and magnetic fields, respectively. The time dependence of the fields includes rapid oscillations at the carrier frequency $\omega_0 = 2\pi c/\lambda_0$, where c is the speed of light in vacuum and λ_0 is the illumination wavelength.

In our simulations, we compute the optical force using the full time-resolved field data generated by a single ultrashort pulse. The electric dipole moment is given by

$$\vec{p}(t) = \alpha(\omega_0)\vec{E}(t), \tag{2}$$

where $\alpha = \alpha' + i\alpha''$ is the complex polarizability, with α' representing the dispersive component and α'' the absorptive component. Since the pulse has a narrow spectral bandwidth, we treat α as frequency-independent.

To extract the net optical effect, we integrate the force over the pulse duration. For reference, in the case of a harmonic field $\vec{E}(t) = \vec{E}_0(\vec{r})e^{i\vec{k}\cdot\vec{r}}$, the time-averaged force separates into gradient and scattering contributions:

$$\langle\vec{F}\rangle = \frac{\alpha'}{2}\sum_i \mathrm{Re}\left\{E_i^*\nabla E_i\right\} + \frac{\alpha''}{2}\sum_i \mathrm{Im}\left\{E_i^*\nabla E_i\right\}. \tag{3}$$

The first term corresponds to the gradient force,

$$\vec{F}_{\mathrm{grad}} = \frac{\alpha'}{4}\nabla|\vec{E}_0|^2, \tag{4}$$

which attracts the particle toward regions of high field intensity.

The second term is the scattering force,

$$\vec{F}_{\mathrm{scat}} = \frac{\alpha}{2}|\vec{E}_0|^2\vec{k}, \tag{5}$$

which pushes the particle along the direction of light propagation due to momentum transfer.

The complex polarizability α of a nanoparticle includes the radiation correction due to scattering losses, as described by Draine's formulation [33]:

$$\alpha = \frac{\alpha_0}{1 - i{k_0}^3\alpha_0/(6\pi\varepsilon_0)}, \tag{6}$$

where $k_0 = 2\pi/\lambda_0$ is the free-space wavenumber, and α_0 is the static polarizability. For a spherical particle, α_0 is given by the Clausius–Mossotti relation [34]:

$$\alpha_0 = 3V\varepsilon_0\frac{\varepsilon_p - \varepsilon_m}{\varepsilon_p + 2\varepsilon_m}, \tag{7}$$

where V is the particle volume, and ε_p, ε_m, and ε_0 are the permittivities of the particle, surrounding medium, and free space, respectively. For small particles such as those used in our study, the quasistatic approximation $\alpha \approx \alpha_0$ is generally sufficient.

For non-spherical particles, such as rods and disks, the polarizability becomes anisotropic and depends on the direction of the applied field. The polarizability component along the i-th principal axis of an ellipsoid is [35]:

$$\alpha_i = V\varepsilon_0\frac{\varepsilon_p - \varepsilon_m}{\varepsilon_m + N_i(\varepsilon_p - \varepsilon_m)}, \tag{8}$$

where N_i is the depolarization factor along that axis. These factors depend solely on the particle geometry and satisfy $N_x + N_y + N_z = 1$.

Assuming the ellipsoid has semi-axes a_x, a_y, and a_z, the depolarization factor in the i-th direction is defined as:

$$N_i = \frac{a_x a_y a_z}{2}\int_0^\infty \frac{ds}{(s + {a_i}^2)\sqrt{(s + {a_x}^2)(s + {a_y}^2)(s + {a_z}^2)}}. \tag{9}$$

In our study, we consider rotationally symmetric cylindrical particles: disks (oblate cylinders) and rods (prolate cylinders), each with uniaxial symmetry. For such particles, the polarizability splits into axial (α_z) and transverse (α_t) components. Using the limiting formulas for high-aspect-ratio cylinders [35], we write:

For rods:

$$\alpha_z = V\varepsilon_0 \frac{\varepsilon_p - \varepsilon_m}{\varepsilon_m}, \quad \alpha_t = 2V\varepsilon_0 \frac{\varepsilon_p - \varepsilon_m}{\varepsilon_p + \varepsilon_m}, \tag{10}$$

For disks:

$$\alpha_z = V\varepsilon_0 \frac{\varepsilon_p - \varepsilon_m}{\varepsilon_p}, \quad \alpha_t = V\varepsilon_0 \frac{\varepsilon_p - \varepsilon_m}{\varepsilon_m}. \tag{11}$$

When the particle is tilted at an angle θ with respect to the electric field direction, the effective polarizability becomes:

$$\alpha_{\text{eff}} = \alpha_z \cos^2\theta + \alpha_t \sin^2\theta, \tag{12}$$

which allows us to model orientation-dependent force responses for anisotropic particles.

The dielectric constants of gold and water at a wavelength of 550 nm were obtained from experimental data: for gold from Johnson and Christy [36], and for water from Hale and Querry [37].

Gold nanoparticles absorb optical energy and can undergo transient heating under pulsed illumination. To quantify the temperature rise associated with the electromagnetic fields used in this work, we evaluate the per-pulse lattice temperature increase directly from the time-resolved FDTD fields.

At each spatial point in the monitor plane, the instantaneous intensity is evaluated as [38]

$$I(\mathbf{r}, t) = \frac{1}{2} n\, \varepsilon_0\, c\, |\mathbf{E}(\mathbf{r}, t)|^2, \tag{13}$$

where n is the refractive index of the background medium. The local fluence per pulse is obtained by time integration,

$$F(\mathbf{r}) = \int I(\mathbf{r}, t)\, dt. \tag{14}$$

The absorbed energy per pulse is estimated using an absorption cross-section formalism [38],

$$E_{\text{abs}}(\mathbf{r}) = \sigma_{\text{abs}}\, F(\mathbf{r}), \tag{15}$$

and the corresponding per-pulse nanoparticle temperature rise is [38,39]

$$\Delta T(\mathbf{r}) = \frac{E_{\text{abs}}(\mathbf{r})}{\rho\, C_p\, V}, \qquad V = \frac{4}{3}\pi R^3. \tag{16}$$

Here R is the nanoparticle radius, ρ is the gold density, and C_p is the gold heat capacity.

The methodology described above enables precise calculation of the time-dependent optical forces acting on anisotropic nanoparticles illuminated by pulsed photonic nanojets and photonic hooks. In the following section, we present the computed field distributions and force maps, and analyze how particle shape, orientation, and medium influence the optical force response.

Closed-form expressions do not exist for the electrostatic polarizability of circular cylinders; it is typically computed numerically [35]. Importantly, the cylinder's polarizability is very close to that of a spheroid with the same permittivity contrast and length-to-diameter ratio, with errors better than ~1% across aspect ratios [35]. Thus, using ellipsoidal depolarization factors, and their high-aspect-ratio limits, for rods (prolate) and disks (oblate) is a standard and accurate approximation for cylinders. In the ellipsoidal picture the special limits are well defined (disk: $N = \{1, 0, 0\}$; needle: $N = \{0, \frac{1}{2}, \frac{1}{2}\}$), which we exploit to construct the axial/transverse components used in Eqs. (10) and 11. For our geometries (rod $h/r \gg 1$, disk $h/r \ll 1$), the parameters fall within these asymptotic regimes; any residual cylinder vs. spheroid discrepancy mainly introduces a weak overall scale factor and does not modify the observed angular trends.

3. Results and discussion

Figure 2 shows the electric field magnitude $|E|$ generated by a dielectric micro-cylinder under pulsed illumination, comparing photonic nanojets (PNJs) and photonic hooks (PHs) in air and water. When transitioning from air to water, the dielectric cylinder geometry and material refractive index are kept fixed, and only the surrounding medium refractive index is varied, enabling a direct comparison under different refractive index contrasts.

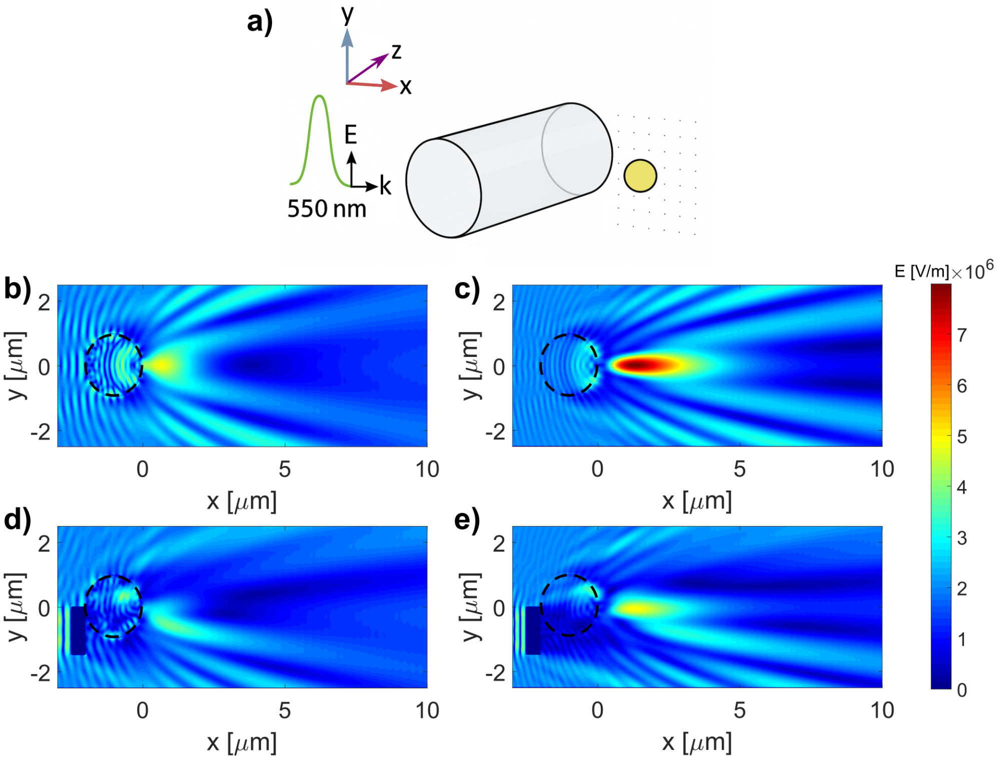

Fig. 2. Electric field magnitude $|E|$ under pulsed illumination at 550 nm: (a) Schematic illustrating the FDTD simulation geometry, including the dielectric cylinder, illumination direction ($\mathbf{k}$), electric field polarization ($\mathbf{E}$), and coordinate axes (x, y, z) (b) photonic nanojet in air, (c) photonic nanojet in water, (d) photonic hook in air, (e) photonic hook in water. The dashed circle marks the cylinder boundary; the black rectangle in (d,e) indicates the metallic plate.

In the absence of the metallic plate (top row), a symmetric PNJ forms in front of the cylinder. The PNJ is narrower and more intense in water [Fig. 2(c)] than in air [Fig. 2(b)], due to the index ratio between the cylinder and the surrounding medium moving closer to the range of approximately 1.2–2 that maximizes near-field focusing in dielectric microcylinders [22]. The transverse confinement of the photonic nanojet was quantified using the FWHM of the intensity profile, defined as $I \propto |E|^2$ and evaluated at the location of maximum intensity. For an illumination wavelength of $\lambda = 550$ nm, the PNJ exhibits a FWHM of 0.758 μm in air and 0.429 μm in water. These correspond to approximately 1.38 λ and 0.78 λ, respectively.

Introducing a metallic plate (bottom row) breaks the field symmetry and generates a photonic hook. In air [Fig. 2(d)], the hook appears more distorted and spatially spread. In contrast, the hook in water [Fig. 2(e)] is sharper, with a higher peak intensity and more confined curvature.

These differences arise from the combined effect of the surrounding refractive index and the boundary conditions imposed by the obstruction. It should be emphasized that the photonic hook represents a locally curved intensity maximum rather than a global beam deflection; momentum conservation is preserved by counter-propagating field components elsewhere in the illumination, and only the region of maximum curvature is relevant for optical force generation.

Thermal effects scale with optical intensity, therefore we quantify nanoparticle heating for the aqueous configurations that yield the highest local field enhancement, namely a PNJ and PH in water (Fig. 2). These two cases bracket the maximum heating observed across all simulations and therefore provide a conservative assessment of thermal effects under the pulse parameters used in this work.

Figure 3 summarizes the corresponding thermal analysis. Panels (a) and (c) show spatial maps of the temperature increase per pulse of nanoparticle $\Delta T(x, y)$ for PNJ and PH in water configurations, respectively, computed directly from the time-resolved FDTD fields. Panels (b) and (d) show $\Delta T(x)$ extracted along a horizontal cut passing through the global maximum of ΔT in each case.

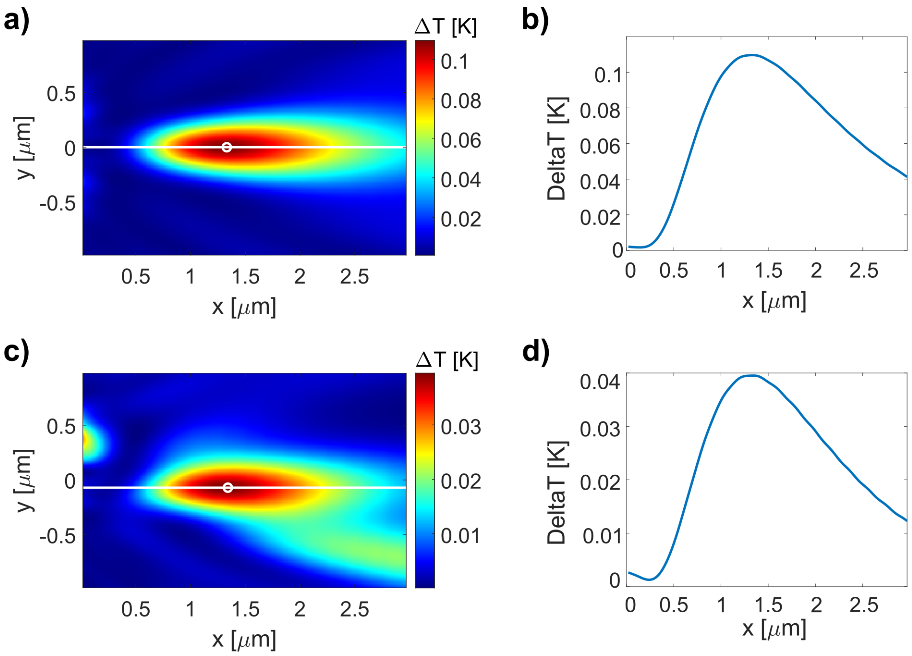

Fig. 3. Nanoparticle temperature rise per pulse calculated from the time-resolved FDTD fields for photonic nanojet (PNJ) and photonic hook (PH) configurations in water. (a) Spatial map of the per-pulse temperature rise $\Delta T(x, y)$ for a PNJ in water; the white line indicates the horizontal cut through the thermal maximum. (b) Corresponding $\Delta T(x)$ profile along the hotspot cut for the PNJ case. (c) Spatial map of $\Delta T(x, y)$ for a PH in water, with the hotspot cut indicated. (d) Corresponding $\Delta T(x)$ profile for the PH case. The PNJ-in-water configuration yields the highest per-pulse temperature rise among all simulated cases, $\Delta T_{\max} = 1.10 \times 10^{-1}$ K, while the PH-in-water configuration reaches $\Delta T_{\max} = 3.95 \times 10^{-2}$ K.

For the PNJ in water configuration [Fig. 3(a,b)], which yields the highest heating among all simulated cases, the maximum per-pulse temperature rise is $\Delta T_{\max} = 1.10 \times 10^{-1}$ K. For the PH in water configuration [Fig. 3(c,d)], the corresponding maximum is lower, $\Delta T_{\max} = 3.95 \times 10^{-2}$ K, reflecting the reduced peak intensity and increased spatial spreading of the photonic hook relative to the nanojet.

Using $\rho = 19300\ \mathrm{kg/m^3}$, $C_p = 129\ \mathrm{J/(kg\,K)}$, and a particle radius of $R = 25$ nm, the gold nanosphere thermal capacity is

$$C_{\mathrm{th}} = \rho C_p V \approx 1.63 \times 10^{-16}\ \mathrm{J/K}, \tag{17}$$

which implies a peak absorbed energy per pulse of

$$E_{\mathrm{abs,max}} = C_{\mathrm{th}} \Delta T_{\mathrm{max}} \approx 1.79 \times 10^{-17}\ \mathrm{J} \tag{18}$$

for the worst case - PNJ in water configuration. At a repetition rate of $f_{\mathrm{rep}} = 100$ MHz, the corresponding average absorbed power is

$$P_{\mathrm{abs}} \approx E_{\mathrm{abs,max}} f_{\mathrm{rep}} \approx 1.8 \times 10^{-9}\ \mathrm{W}. \tag{19}$$

To justify the lumped-temperature approximation implicit in Eq. (16), we evaluate the Biot number, which compares internal heat conduction within the particle to heat transfer across its boundary. Approximating the interfacial heat transfer coefficient as $h \sim k_m/R$ for conduction into a surrounding medium of thermal conductivity k_m, and using the characteristic length $L_c = V/A = R/3$ for a sphere, we obtain [40]

$$\mathrm{Bi} \approx \frac{h L_c}{k_{\mathrm{Au}}} \approx \frac{k_m}{3 k_{\mathrm{Au}}}. \tag{20}$$

For water, with $k_m \approx 0.61\ \mathrm{W/(m\,K)}$ and $k_{\mathrm{Au}} \approx 320\ \mathrm{W/(m\,K)}$, this yields $\mathrm{Bi} \approx 6.3 \times 10^{-4} \ll 0.1$, confirming that the nanoparticle remains internally isothermal during heating and cooling.

We further estimate the conduction-limited cooling time of a spherical nanoparticle in a surrounding medium as [39]

$$\tau_{\mathrm{np}} \sim \frac{\rho C_p R^2}{3 k_m}. \tag{21}$$

For $R = 25$ nm in water, $\tau_{\mathrm{np}} \approx 8.6 \times 10^{-10}$ s, which is more than an order of magnitude shorter than the interpulse separation of 10 ns at 100 MHz. A conservative bound on steady-state heating in water is therefore

$$\Delta T_{\mathrm{ss}} \sim \frac{P_{\mathrm{abs}}}{4\pi k_m R} \approx 9.5 \times 10^{-3}\ \mathrm{K}, \tag{22}$$

indicating negligible thermal accumulation under the studied conditions.

This analysis provides a quantitative upper bound on both per-pulse and cumulative nanoparticle heating implied by the electromagnetic fields used in this work. Under the investigated pulse parameters, thermo-driven effects such as vapor bubble formation, convection, or thermophoresis are therefore not expected to dominate the observed nanoparticle dynamics. A fully coupled thermo-fluidic treatment is beyond the scope of the present study.

Having established that thermal effects remain negligible, we now examine the resulting optical forces on nanoparticles of different geometries. Figure 4 shows the calculated optical force magnitude on a sphere, disk, and rod placed in the photonic hook field, in air (top row) and water (bottom row).

In both environments, the optical impulse distribution depends strongly on particle geometry. In air [Fig. 4(a-c)], the sphere exhibits the largest and most localized impulse near the photonic hook trajectory. The rod shows a weaker, more spatially distributed impulse pattern, while the disk yields the smallest response across the plotted region. In water [Fig. 4(d-f)], the impulse becomes markedly stronger and more confined, and the sphere again produces the dominant field. The disk shows a moderate increase relative to air but remains substantially weaker than

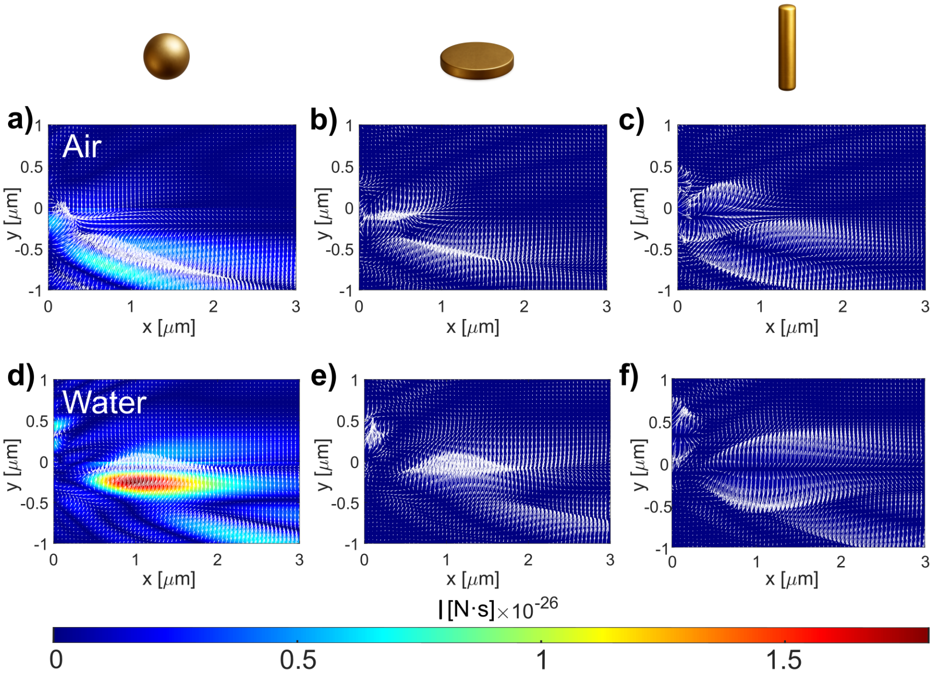

Fig. 4. Optical force magnitude acting on nanoparticles of different geometries under photonic hook illumination. (a–c) Force distributions in air for a sphere, disk, and rod, respectively. (d–f) Corresponding force distributions in water. In both media, all particles have identical volume. The color scale shows the time-integrated optical force (impulse), $\mathbf{I} = \int \mathbf{F}(t)\,dt$, corresponding to the momentum transfer per pulse.

the sphere, and the rod exhibits the weakest impulse response in water. Overall, Fig. 4 indicates that, for the parameters used here, the spherical particle couples most efficiently to the PH field in both media, while anisotropic shapes (disk and rod) produce weaker impulse transfer and more fragmented spatial patterns. This highlights that geometry and surrounding medium jointly control not only the magnitude but also the spatial localization and directionality of momentum transfer per pulse under structured illumination.

Unlike spheres, the anisotropic geometry of rods and disks results in orientation-dependent optical behavior, where both the magnitude and direction of the optical force can vary significantly with the particle's tilt relative to the incident electric field. To investigate this effect, we analyze the optical force magnitude acting on disk- and rod-shaped gold nanoparticles under both PNJ and PH illumination in water, as a function of their orientation angle.

Figure 5 shows the force distributions under PH illumination. The top row illustrates the optical force magnitude on a disk at $\theta = 0°$, 45°, and 90°. At $\theta = 0°$, the electric field is aligned with the disk's axial (thickness) direction, which exhibits weak polarizability, resulting in minimal optical force. As the tilt angle increases, the projection of the more strongly polarizable transverse axis onto the electric field becomes more significant, leading to a monotonic increase in force that peaks at $\theta = 90°$.

The bottom row shows the corresponding force distributions for a rod. At $\theta = 0°$, the rod's long axis is aligned with the electric field, maximizing coupling to its dominant axial polarizability and resulting in the strongest optical force. Although the global incident polarization is along $\hat{y}$, the local electric field in the photonic hook region is highly nonuniform and exhibits substantial $\hat{x}$- and $\hat{z}$-components due to beam curvature and focusing. The dominant local field near the particle

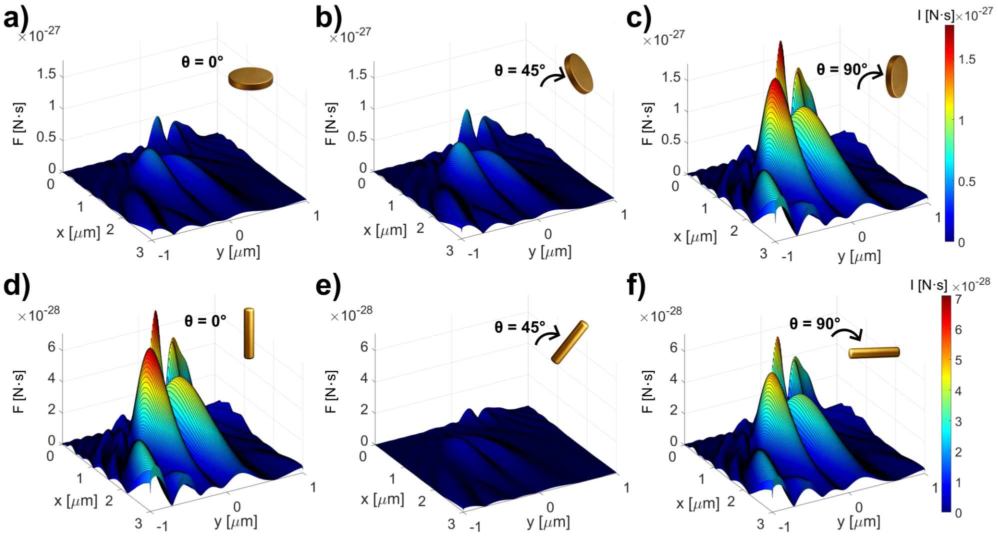

Fig. 5. Orientation dependence of optical forces under photonic hook illumination in water. (a–c) Optical force magnitude on a disk-shaped nanoparticle at $\theta = 0°$, 45°, and 90°, respectively. (d–f) Corresponding force distributions for a rod-shaped nanoparticle at the same tilt angles. The color scale shows the time-integrated optical force (impulse), $\mathbf{I} = \int \mathbf{F}(t)\,\mathrm{d}t$, corresponding to the momentum transfer per pulse.

is tilted toward $\hat{z}$, so when the rod is oriented along $\hat{z}$ ($\theta = 0°$), it couples most efficiently to this high-intensity region, yielding the strongest optical force despite the nominal $\hat{y}$-polarization of the incident beam. At $\theta = 45°$, the field is equally projected onto both the strong axial and weak transverse directions, leading to a minimum in force due to polarizability dilution. At $\theta = 90°$, the transverse face aligns with the field, restoring some force but not reaching the level observed at $\theta = 0°$.

The force minima observed at intermediate particle orientations in Fig. 5 arise from the angular projection of the anisotropic polarizability tensor onto the local electromagnetic field. For rods and disks, the induced dipole moment is governed by longitudinal and transverse polarizabilities, whose relative contributions vary with orientation. At intermediate angles, neither component is maximally aligned with the dominant field direction, leading to a reduced effective polarizability and a minimum in the optical force.

To compare with the symmetric field configuration, we examine the same particle orientations under PNJ illumination. Figure 6 shows the force distributions for disk- and rod-shaped nanoparticles in water at $\theta = 0°$, 45°, and 90°. The disk again shows a monotonic increase in force with tilt angle, reaching a maximum when the transverse face is aligned with the electric field at $\theta = 90°$. The rod exhibits its highest force at $\theta = 0°$, followed by a sharp decrease at $\theta = 45°$ due to polarizability dilution, and a partial recovery at $\theta = 90°$. Compared to the PH case, the PNJ produces stronger and more symmetric force distributions, especially for the rod at small tilt angles, owing to the spatial uniformity of the structured field.

To further quantify the orientation dependence, we extract the maximum optical force magnitude as a function of tilt angle θ for disk- and rod-shaped nanoparticles in water under both PNJ and PH illumination. Figure 7 presents the results, with solid lines representing PNJ and dashed lines representing PH. For the disk (blue curves), the optical force is minimal at $\theta = 30°$, where the electric field is neither fully aligned with the weak axial direction nor fully projected onto the highly polarizable transverse face. As the tilt increases beyond this point, the transverse

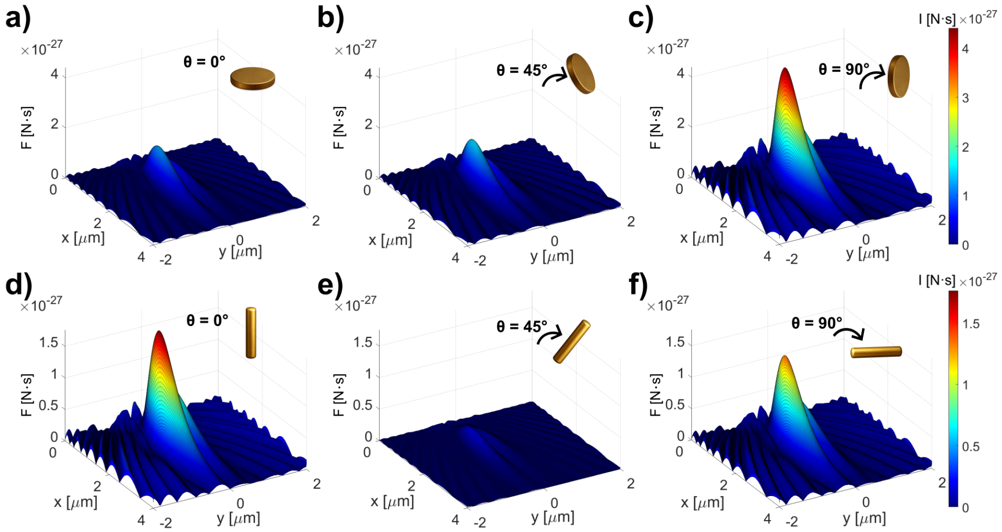

Fig. 6. Orientation dependence of optical forces under photonic nanojet illumination in water. (a–c) Optical force magnitude on a disk-shaped nanoparticle at $\theta = 0°$, 45°, and 90°, respectively. (d–f) Corresponding force distributions for a rod-shaped nanoparticle. The color scale shows the time-integrated optical force (impulse), $\mathbf{I} = \int \mathbf{F}(t)\,\mathrm{d}t$, corresponding to the momentum transfer per pulse

component dominates, leading to a steady rise in force that peaks at $\theta = 90°$ when the flat face aligns with the field. For the rod (orange curves), the force is maximal at $\theta = 0°$, where the long axis aligns with the electric field and the strong axial polarizability dominates. As the tilt increases, the field projects across both strong and weak axes. At $\theta = 45°$, the rod exhibits a minimum in force due to polarizability dilution, where the effective interaction is split between orthogonal directions. Beyond this angle, the transverse axis increasingly contributes, and the force rises again toward $\theta = 90°$. The force minima observed at intermediate orientations are expected, as the phase and amplitude of scattering and absorption by anisotropic particles are inherently angle-dependent, leading to reduced coupling between the incident field and specific polarizability components at certain orientations. In addition, PNJ consistently yields stronger optical forces than PH across all angles and geometries. This difference arises from the PNJ's higher intensity and tighter field confinement compared to the broader, curved profile of the PH. These results emphasize how both field structure and particle orientation interact to determine the optical force landscape for anisotropic nanoparticles.

To better understand the orientation-dependent trends in optical force, we examine the effective complex polarizability of the nanoparticles as a function of tilt angle. Figure 8 shows the real (α') and imaginary (α'') parts of the effective polarizability α_{eff} for rod- and disk-shaped particles in water, obtained by projecting their anisotropic polarizability tensors onto the incident electric field. The gradient force, governed by α', dictates the angular dependence and the consistently stronger PNJ response compared to PH. The scattering contribution, governed by α'', primarily adjusts the force magnitude without altering the angular extrema. This separation is evident in Fig. 8, where variations in α' with tilt correspond closely to the maxima and minima observed in Fig. 7.

As described in Eq. (3), the real part α' governs the gradient force, which draws particles toward regions of high field intensity, while the imaginary part α'' governs the scattering force, associated with momentum transfer along the propagation direction.

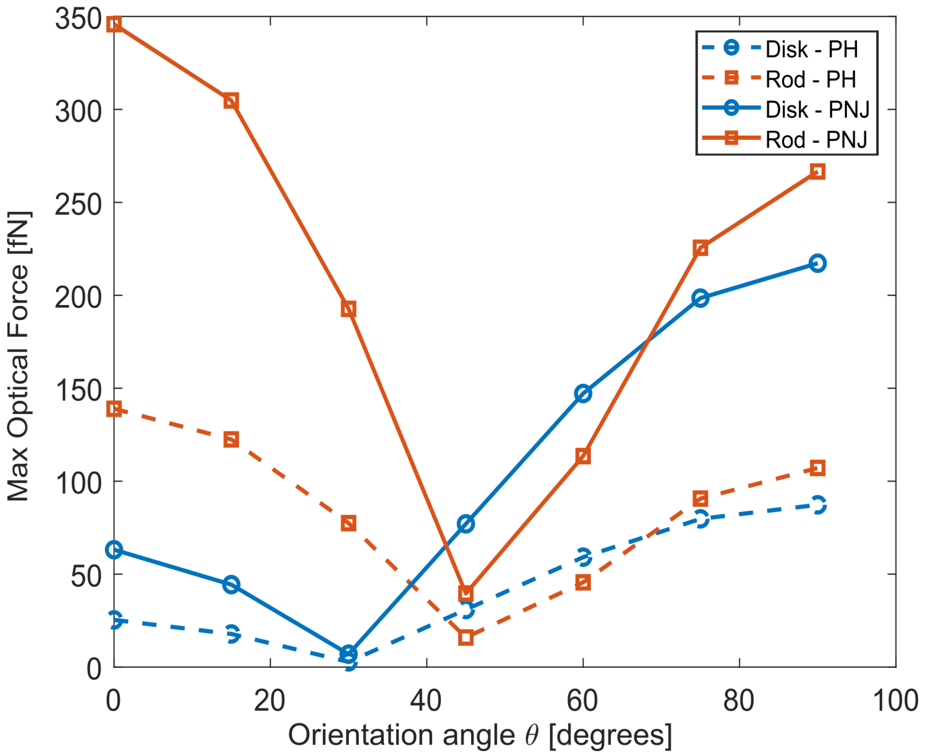

Fig. 7. Maximum optical force magnitude versus orientation angle θ under PNJ and PH illumination in water. Solid lines: PNJ. Dashed lines: PH. Orange: rod-shaped nanoparticle. Blue: disk-shaped nanoparticle.

For the disk (blue curves), α' decreases monotonically with increasing tilt, becoming more negative as the field projection shifts from the weak axial direction to the strongly polarizable transverse face. α'' increases gradually with tilt, reflecting stronger absorption and energy dissipation. However, despite these monotonic trends in polarizability, the optical force shows a non-monotonic dependence (Fig. 7). Specifically, the force first decreases from 0° to 30°, reaching a local minimum, and only then begins to rise toward a maximum at 90°. While polarizability plays a central role, the spatial structure and gradients of the field also influence the force profile, especially under structured illumination like PNJs and PHs, where the field distribution varies across the particle's extent.

For the rod (orange curves), α' exhibits a non-monotonic behavior: it is strongly negative at $\theta = 0°$, crosses zero near $\theta = 45°$, and becomes increasingly positive at higher angles. This behavior aligns with the force minimum at $\theta = 45°$ in Fig. 7, corresponding to a condition where the electric field couples equally to both strong and weak polarizability axes. This results in destructive interference and reduced net coupling. Meanwhile, α'' varies only modestly with tilt and plays a secondary role, modulating the magnitude of the scattering force without altering the overall trend.

At $E_0 = 2\ \mathrm{MV\,m^{-1}}$, the corresponding peak intensity is $I_{\mathrm{peak}} = \frac{1}{2} c\varepsilon_0 E_0^2 \approx 5.3 \times 10^9\ \mathrm{W\,cm^{-2}}$ and an average power of ~ 5 mW for 100 fs pulses at a 100 MHz repetition rate, assuming a beam area of 10 $\mu\mathrm{m}^2$. Under these illumination conditions, the peak optical forces per pulse reach 1.5×10^{-13} N (sphere, $r = 25$ nm), 1.4×10^{-13} N (rod, 0°), and 2.5×10^{-14} N (disk, 0°). For reference, normalizing the peak forces to the time-averaged local optical intensity at

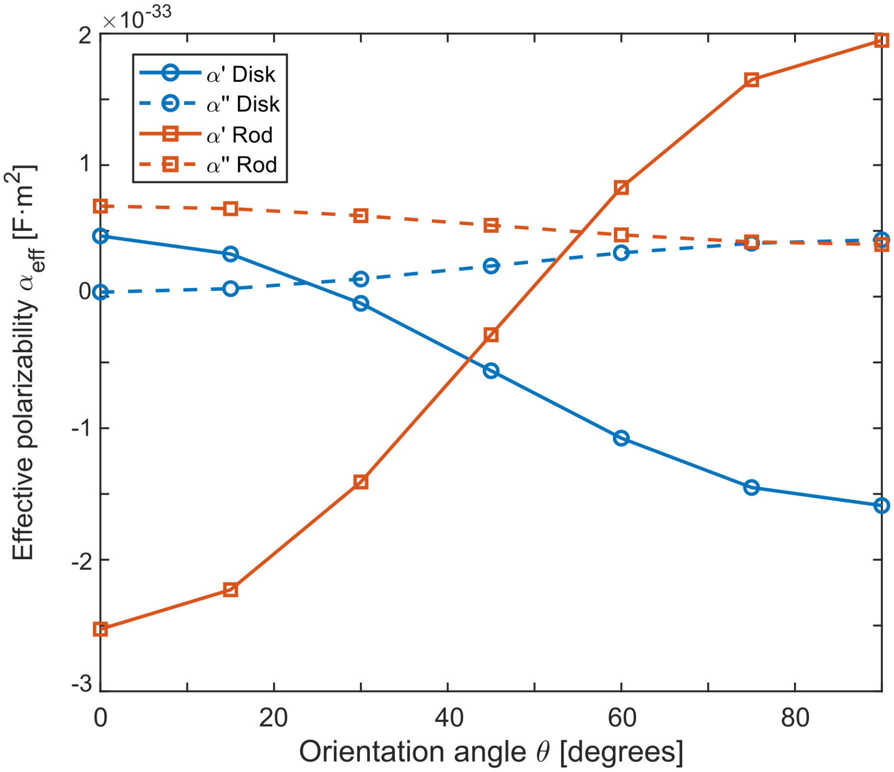

Fig. 8. Effective polarizability α_{eff} as a function of orientation angle θ for disk (blue) and rod (orange) nanoparticles in water. Solid lines: real part α'. Dashed lines: imaginary part α''.

the particle position yields an effective force-to-power ratio on the order of 10^2–10^3 pN/W, comparable to values reported for near-field and plasmonic optical manipulation schemes, while operating at sub-microwatt average powers. Considering the viscous drag for motion in water at $v = 1\ \mu\mathrm{m\,s}^{-1}$ is $F_{\mathrm{drag}} = \gamma v$, with $\gamma = 6\pi\eta r_{\mathrm{eff}}$ and $\eta = 10^{-3}\,\mathrm{Pa{\cdot}s}$. Using $r_{\mathrm{eff}} = 25$ nm yields $F_{\mathrm{drag}} \approx 4.7 \times 10^{-16}$ N, so the instantaneous optical force during a pulse exceeds the drag benchmark by factors of ~ 60–320 (geometry dependent).

The force calculations are evaluated at fixed particle orientations and are not intended to represent long-time rotational equilibrium. Instead, the force-angle dependence characterizes how the instantaneous translational optical force varies with particle orientation under structured pulsed illumination. In practice, anisotropic particles may rotate between pulses or during extended exposure, but the present analysis isolates the orientation-dependent force response itself, which is a prerequisite for any coupled force-torque or dynamical treatment.

Compared to continuous-wave illumination, ultrashort-pulse excitation provides strong instantaneous field gradients that enhance the gradient-to-scattering force ratio while minimizing cumulative heating. The 10 ns separation between consecutive 100 MHz pulses far exceeds the nanoparticle cooling time (tens to hundreds of picoseconds [18,20]), enabling full thermal relaxation. This approach is advantageous for thermally sensitive or aqueous systems and supports potential applications in pulsed optical trapping, directed nanoparticle transport, and ultrafast laser nanoprinting.

Each pulse transfers an impulse $J_{\mathrm{opt}} \approx F_{\max}\tau_{\mathrm{eff}}$, where $\tau_{\mathrm{eff}} = T_{\mathrm{FWHM}}\sqrt{\pi/(4\ln 2)} \approx 1.06 \times 10^{-13}$ s for a 100 fs Gaussian. This gives $J_{\mathrm{opt}} \sim (0.3\text{–}1.6) \times 10^{-26}$ N·s across our geometries. The Brownian impulse over the same interval, $J_B = \sqrt{2k_BT\,\gamma\,\Delta t}$ with $\Delta t = 100$ fs, is $\sim (6 \pm 1) \times 10^{-22}$ N·s, i.e., four orders of magnitude larger. A single ultrashort pulse therefore cannot deterministically translate a nanoparticle; instead, it biases the stochastic motion (Table 1).

Table 1. Maximum instantaneous optical forces $F_{\max}$ at $E_0 = 2$ MV m^{-1} under pulsed illumination (100 fs) for representative geometry–orientation pairs. Viscous drag benchmark in water at $v = 1\ \mu$m s^{-1} is $F_{\mathrm{drag}} = \gamma v \approx 0.47$ fN (using $r_{\mathrm{eff}} = 25$ nm)

Particle / Field	Orientation	$F_{\max}$ [fN]	Factor over F_{drag}
Sphere (PH)	–	215	~ 460
Sphere (PNJ)	–	379	~ 800
Rod (PH)	0°	139	~ 300
Rod (PNJ)	0°	346	~ 740
Disk (PH)	90°	87.3	~ 190
Disk (PNJ)	90°	217	~ 460

For a pulse train, the bias accumulates: the cycle-averaged force is $\langle F\rangle = f\,J_{\mathrm{opt}}$, and the mean drift velocity is $v = \langle F\rangle/\gamma$. At $E_0 = 2$ MV m^{-1} and $f = 100$ MHz, the drift is only a few nm s^{-1} in water, so short-time trajectories appear diffusion-dominated. Because $F_{\max}$ and J_{opt} scale as E_0^2, the drift increases quadratically with field amplitude and linearly with repetition rate; operating at higher E_0 and/or f provides a practical route to measurable bias while retaining a low duty cycle.

4. Conclusions

We presented a comprehensive computational study of optical forces on spherical and anisotropic gold nanoparticles, rods and disks, illuminated by ultrashort pulsed photonic nanojets (PNJs) and photonic hooks (PHs). Using full 3D FDTD simulations and analytical modeling of anisotropic polarizability, we evaluated how particle shape, orientation, and surrounding medium govern the optical force landscape.

Our results show that non-spherical particles exhibit sharp orientation-dependent behavior, driven by their anisotropic polarizability. For rods, the optical force peaks at $\theta = 0°$ when the long axis aligns with the electric field and drops sharply at $\theta = 45°$ due to polarizability dilution, a condition where the field projects equally onto weak and strong axes. For disks, the force displays a non-monotonic trend with a minimum at $\theta = 30°$ and a peak at $\theta = 90°$, reflecting the tradeoff between axial and transverse coupling. These trends correlate well with the real part of the effective polarizability α', which governs the gradient force, while the imaginary part α'' modulates the scattering component.

We further demonstrated that the surrounding medium strongly influences optical manipulation efficiency. In water, the higher refractive index contrast sharpens and intensifies both the PNJ and PH fields. Additionally, the force magnitude depends on both particle geometry and the surrounding medium, with spherical nanoparticles exhibiting the strongest momentum transfer in both air and water, while anisotropic particles show weaker and more spatially distributed responses. We emphasize that the reported forces correspond to impulsive, non-equilibrium optical manipulation rather than steady-state trapping.

Beyond the specific findings, this study underscores a key insight for real-world applications: nanoparticles are rarely perfect spheres and often operate in aqueous environments. The strong dependence of optical forces on both geometry and orientation highlights the importance of modeling realistic particle shapes and accounting for medium effects when designing optical manipulation strategies. Our results offer theoretical guidance for optimizing nanoparticle control in biomedical, sensing, and nanofabrication applications, particularly in systems employing structured optical fields for high precision manipulation. These capabilities are directly relevant to biosensing, where orientation-sensitive nanoparticles can enhance signal specificity, to drug delivery, where pulsed structured fields may enable controlled release at the nanoscale, and to 3D nanoprinting, where geometry and orientation-dependent forces provide a pathway for assembling anisotropic building blocks with high precision.

Funding. Israel Science Foundation (1023/24).

Acknowledgment. The authors thank Dr. Aviad Katiyi for assistance in preparing the rendered figures.

Disclosures. The authors declare that they have no known competing financial interests or personal relationships that could have appeared to influence the work reported in this paper.

Data availability. Data underlying the results presented in this paper are not publicly available at this time but may be obtained from the authors upon reasonable request.

References

1. A. Ashkin, J. M. Dziedzic, and T. Yamane, “Optical trapping and manipulation of single cells using infrared laser beams,” Nature **330**(6150), 769–771 (1987).
2. A. Karabchevsky, T. Elbaz, A. Katiyi, *et al.*, “Super-resolution imaging and optomechanical manipulation using optical nanojet for nondestructive single-cell research,” Adv. Photonics Res. **3**(2), 2100233 (2022).
3. J. E. Baker, R. P. Badman, and M. D. Wang, “Nanophotonic trapping: precise manipulation and measurement of biomolecular arrays,” Wiley Interdiscip. Rev.: Nanomed. Nanobiotechnol. **10**, e1477 (2018).
4. M. Dienerowitz, M. Mazilu, and K. Dholakia, “Optical manipulation of nanoparticles: a review,” J. Nanophotonics **2**(1), 021875 (2008).
5. J. Qin, X. Wu, A. Krueger, *et al.*, “Light-driven plasmonic microrobot for nanoparticle manipulation,” Nat. Commun. **16**(1), 2570 (2025).
6. S. Ghosh and A. Ghosh, “All optical dynamic nanomanipulation with active colloidal tweezers,” Nat. Commun. **10**(1), 4191 (2019).
7. J. D. Kolbow, N. C. Lindquist, C. T. Ertsgaard, *et al.*, “Nano-optical tweezers: Methods and applications for trapping single molecules and nanoparticles,” ChemPhysChem **22**(14), 1409–1420 (2021).
8. D. G. Kotsifaki and S. Nic Chormaic, “Plasmonic optical tweezers based on nanostructures: fundamentals, advances and prospects,” Nanophotonics **8**(7), 1227–1245 (2019).
9. Y. Zhang, C. Min, X. Dou, *et al.*, “Plasmonic tweezers: for nanoscale optical trapping and beyond,” Light:Sci. Appl. **10**(1), 59 (2021).
10. M. Righini, A. S. Zelenina, C. Girard, *et al.*, “Parallel and selective trapping in a patterned plasmonic landscape,” Nat. Phys. **3**(7), 477–480 (2007).
11. J. Berthelot, S. S. Aćimović, M. L. Juan, *et al.*, “Three-dimensional manipulation with scanning near-field optical nanotweezers,” Nat. Nanotechnol. **9**(4), 295–299 (2014).
12. A. Kotnala and R. Gordon, “Quantification of high-efficiency trapping of nanoparticles in a double nanohole optical tweezer,” Nano Lett. **14**(2), 853–856 (2014).
13. M. L. Juan, M. Righini, and R. Quidant, “Plasmon nano-optical tweezers,” Nat. Photonics **5**(6), 349–356 (2011).
14. A. Grigorenko, N. Roberts, M. Dickinson, *et al.*, “Nanometric optical tweezers based on nanostructured substrates,” Nat. Photonics **2**(6), 365–370 (2008).
15. Y.-F. Chen, X. Serey, R. Sarkar, *et al.*, “Controlled photonic manipulation of proteins and other nanomaterials,” Nano Lett. **12**(3), 1633–1637 (2012).
16. Y. Ren, Q. Chen, M. He, *et al.*, “Plasmonic optical tweezers for particle manipulation: principles, methods, and applications,” ACS Nano **15**(4), 6105–6128 (2021).
17. Y. Shi, Q. Song, I. Toftul, *et al.*, “Optical manipulation with metamaterial structures,” Appl. Phys. Rev. **9**(3), 031303 (2022).
18. M. Gandolfi, A. Crut, F. Medeghini, *et al.*, “Ultrafast thermo-optical dynamics of plasmonic nanoparticles,” J. Phys. Chem. C **122**(15), 8655–8666 (2018).
19. T. Stoll, P. Maioli, A. Crut, *et al.*, “Advances in femto-nano-optics: ultrafast nonlinearity of metal nanoparticles,” Eur. Phys. J. B **87**(11), 260 (2014).
20. M. Spector, A. S. Ang, O. V. Minin, *et al.*, “Temperature mediated ‘photonic hook’nanoparticle manipulator with pulsed illumination,” Nanoscale Adv. **2**(6), 2595–2601 (2020).
21. Z. Chen, A. Taflove, and V. Backman, “Photonic nanojet enhancement of backscattering of light by nanoparticles: a potential novel visible-light ultramicroscopy technique,” Opt. Express **12**(7), 1214–1220 (2004).
22. B. S. Luk’yanchuk, R. Paniagua-Domínguez, I. Minin, *et al.*, “Refractive index less than two: photonic nanojets yesterday, today and tomorrow,” Opt. Mater. Express **7**(6), 1820–1847 (2017).
23. A. Kovrov, A. Novitsky, A. Karabchevsky, *et al.*, “A photonic nanojet as tunable and polarization-sensitive optical tweezers,” Ann. Phys. **530**(9), 1800129 (2018).

24. Y.-C. Li, H.-B. Xin, H.-X. Lei, *et al.*, “Manipulation and detection of single nanoparticles and biomolecules by a photonic nanojet,” Light:Sci. Appl. **5**(12), e16176 (2016).
25. H. Wang, X. Wu, and D. Shen, “Trapping and manipulating nanoparticles in photonic nanojets,” Opt. Lett. **41**(7), 1652–1655 (2016).
26. X. Cui, D. Erni, and C. Hafner, “Optical forces on metallic nanoparticles induced by a photonic nanojet,” Opt. Express **16**(18), 13560–13568 (2008).
27. L. Yue, O. V. Minin, Z. Wang, *et al.*, “Photonic hook: a new curved light beam,” Opt. Lett. **43**(4), 771–774 (2018).
28. L. Ling, H.-L. Guo, X.-L. Zhong, *et al.*, “Manipulation of gold nanorods with dual-optical tweezers for surface plasmon resonance control,” Nanotechnology **23**(21), 215302 (2012).
29. J. Li, H. Guo, and Z.-Y. Li, “Microscopic and macroscopic manipulation of gold nanorod and its hybrid nanostructures,” Photonics Res. **1**(1), 28–41 (2013).
30. M. Pelton, M. Liu, H. Y. Kim, *et al.*, “Optical trapping and alignment of single gold nanorods by using plasmon resonances,” Opt. Lett. **31**(13), 2075–2077 (2006).
31. K. Toussaint Jr, M. Liu, M. Pelton, *et al.*, “Plasmon resonance-based optical trapping of single and multiple au nanoparticles,” Opt. Express **15**(19), 12017–12029 (2007).
32. L. Amato, S. S. Keller, A. Heiskanen, *et al.*, “Fabrication of high-aspect ratio su-8 micropillar arrays,” Microelectron. Eng. **98**, 483–487 (2012).
33. B. T. Draine, “The discrete-dipole approximation and its application to interstellar graphite grains,” Astrophysical Journal, Part 1 (ISSN 0004-637X). **333**, 848–872 (1988).
34. J. D. Jackson, *Classical electrodynamics* (John Wiley & Sons, 2021).
35. J. Venermo and A. Sihvola, “Dielectric polarizability of circular cylinder,” J. Electrost. **63**(2), 101–117 (2005).
36. P. B. Johnson and R.-W. Christy, “Optical constants of the noble metals,” Phys. Rev. B **6**(12), 4370–4379 (1972).
37. G. M. Hale and M. R. Querry, “Optical constants of water in the 200-nm to 200-μm wavelength region,” Appl. Opt. **12**(3), 555–563 (1973).
38. G. Baffou and R. Quidant, “Thermo-plasmonics: using metallic nanostructures as nano-sources of heat,” Laser & Photonics Reviews **7**(2), 171–187 (2013).
39. G. Baffou and H. Rigneault, “Femtosecond-pulsed optical heating of gold nanoparticles,” Phys. Rev. B **84**(3), 035415 (2011).
40. O. Ekici, R. Harrison, N. Durr, *et al.*, “Thermal analysis of gold nanorods heated with femtosecond laser pulses,” J. Phys. D: Appl. Phys. **41**(18), 185501 (2008).